AIAA '89

AIAA 89-0338
Navier-Stokes Solutions about the F/A-18 Forebody-LEX Configuration

F. Ghaffari and B. Bates, Vigyan Research Associates, Hampton, VA;
J. Luckring and J. Thomas, NASA-Langley, Hampton, VA

27th Aerospace Sciences Meeting
January 9-12, 1989/Reno, Nevada

Navier-Stokes Solutions about the F/A-18 Forebody-LEX Configuration

Farhad Ghaffari[†]
Vigyan Research Associates
James M. Luckring[‡]
NASA-Langley Research Center
James L. Thomas[§]
NASA-Langley Research Center
Brent L. Bates[#]
Vigyan Research Associates
Hampton, Virginia

Abstract

Three-dimensional viscous flow computations are presented for the F/A-18 forebody-LEX geometry. Solutions are obtained from an algorithm for the compressible Navier-Stokes equations which incorporates an upwind-biased, flux-difference-splitting approach along with longitudinally-patched grids. Results are presented for both laminar and fully turbulent flow assumptions and include correlations with wind tunnel as well as flight-test results. A good quantitative agreement for the forebody surface pressure distribution is achieved between the turbulent computations and wind tunnel measurements at $M_\infty = 0.6$. The computed turbulent surface flow patterns on the forebody qualitatively agree well with in-flight surface flow patterns obtained on an F/A-18 aircraft at $M_\infty = 0.34$.

Nomenclature

C_D	drag coefficient, Drag/ $q_\infty S_{ref}$
C_L	lift coefficient, Lift/ $q_\infty S_{ref}$
C_p	pressure coefficient, $(p - p_\infty)/q_\infty$
c_p	specific heat at constant pressure
c_v	specific heat at constant volume
$\bar{c}$	mean aerodynamic chord of reference wing planform, 8.294 in.
E	total energy per unit volume
$\hat{F}, \hat{G}, \hat{H}$	flux vectors
H	total enthalpy per unit volume
J	Jacobian of the coordinate transformation
k	conductivity
M	Mach number
Pr	Prandtl number
$\hat{Q}$	state vector, $J^{-1}[\rho, \rho u, \rho v, \rho w, e]^T$

q	total velocity
q_∞	freestream dynamic pressure
$R_{\bar{c}}$	Reynolds number based on $\bar{c}$
S_{ref}	area of reference wing planform, extended to configuration centerline
u, v, w	body-axis Cartesian velocity components
v^*	wall-friction velocity, $\sqrt{\tau_w/\rho}$
y/s	fraction of LEX exposed semispan
y^+	inner-law variable, yv^*/ν
α	angle of attack, degrees
γ	ratio of specific heats, c_p/c_v
μ	viscosity
ν	kinematic viscosity, μ/ρ
θ	azimuthal angle
ξ, η, ς	body-fitted coordinates
ρ	density
τ_w	wall shear stress

Subscripts

ℓ	laminar
t	turbulent
v	viscous
∞	freestream reference conditions

[†]Research Engineer, Senior member AIAA

[‡]Research Engineer, Member AIAA

[§]Senior Research Scientist, Associate Fellow AIAA

[#]Research Engineer, Member AIAA

Introduction

Advances in numerical solution methodology along with increased computer speed and capacity have made it feasible to seek numerical solutions to the three-dimensional Navier-Stokes equations for relatively complicated geometries. Prior computations for isolated wing[1,2,3] or body[4,5,6] geometries have demonstrated that accurate Navier-Stokes solutions are not limited to benign flow conditions; converged results can be obtained which include complex flow structures (e.g., three-dimensional separation, shocks, vortices, etc.) as well as interactions among these structures.

Applications to aircraft configurations have been

less forthcoming primarily due to complexities associated with grid generation and surface definition along with the relatively large computational resources required for these cases. None the less, recent progress has been shown for several cases including supersonic inviscid flow about the F/A-18 forebody-LEX and the SR-71[7] as well as transonic viscous flow about the F-16A[8]. Most recently, viscous flow computations about the ascent configuration of the space shuttle[9] have demonstrated good correlation with flight data at subsonic, transonic, and supersonic speeds.

The present investigation is directed toward applying an extended version of an implicit Navier-Stokes algorithm[1,3,6] to the F/A-18 forebody-LEX geometry at conditions suitable to the formation of separated subsonic and, in some cases, transonic flows. The extension to the algorithm permits longitudinally-blocked grids which are necessary for accurately modeling the subject configuration. The F/A-18 has been selected for this study primarily due to the availability of current wind-tunnel[10] as well as flight research[11] data related to an ongoing high angle-of-attack research program being conducted by NASA.

The computations are focused on two specific flow conditions in accordance with the recent wind-tunnel and flight-test research. The wind tunnel conditions are $M_\infty = 0.6$, $R_{\bar{c}} = 0.8 \times 10^6$, and $\alpha = 20°$ which correspond to recent tests conducted at the David Taylor Research Center (DTRC) 7x10 foot tunnel with a 6% F/A-18 model. At these conditions the forebody flow could be transitional, hence both laminar as well as turbulent solutions are obtained. The flight conditions are $M_\infty = 0.34$, $R_{\bar{c}} = 13.5 \times 10^6$, and $\alpha = 19°$ which correspond to recent flight tests of the NASA F/A-18 High Alpha Research Vehicle (HARV) conducted at the Dryden Flight Research Facility. At these conditions only turbulent solutions are obtained, but grid sensitivity is addressed.

Governing Equations

The governing equations as well as computational method for the present investigation have been published many times in the open literature[1,3,6] as they have evolved. The flow is presumed to be governed by the unsteady Reynolds-averaged Navier-Stokes equations which are written in a body-fitted coordinate system. They are written in a usual conservation-law form as

$$\hat{Q}_{,t} + (\hat{F} - \hat{F}_v)_{,\xi} + (\hat{G} - \hat{G}_v)_{,\eta} + (\hat{H} - \hat{H}_v)_{,\zeta} = 0$$

Here the subscripts with a comma denote partial differentiation, the subscript v identifies the viscous terms, and the superscript ^ indicates scaling with respect to

the Jacobian of the coordinate transformation. Details for these terms are included in Appendix 1. With the ideal gas assumption, the pressure and total enthalpy can be expressed as

$$p = (\gamma - 1)(E - \frac{1}{2}\rho q^2) \quad ; \quad H = \frac{\gamma}{\gamma - 1}p + \frac{1}{2}\rho q^2$$

For the present study, the thin layer approximation to the governing equations is invoked

$$\hat{F}_v = \hat{G}_v = 0$$

thus accounting for viscous flux terms only in the ζ direction (normal to the body).

Turbulence effects are accounted for through the notion of an eddy viscosity and eddy conductivity.

$$\mu = \mu_\ell + \mu_t = \mu_\ell(1 + \mu_t/\mu_\ell)$$
$$k = k_\ell + k_t = k_\ell(1 + k_t/k_\ell)$$
$$= \frac{c_p \mu_\ell}{Pr_\ell}\left(1 + \frac{\mu_t Pr_\ell}{\mu_\ell Pr_t}\right)$$

The algebraic turbulence model developed by Baldwin and Lomax[12] is used to evaluate appropriate turbulence quantities. For separated flow regions, the notions of Degani and Schiff[13] are drawn upon to determine proper turbulence length scales. A recent extension to this fairly standard approach has been given by Hartwich[14] for massively separated and transitional flows.

Computational Method

Discretization of the governing equations results in a consistent approximation to the conservation laws in integral form

$$\frac{\partial}{\partial t}\int\int\int \hat{Q}\,dV + \int\int \vec{\hat{f}} \cdot \hat{n}\,dS = 0$$

where the time rate of change of the state vector $\hat{Q}$ within a cell is balanced by the net flux $\vec{\hat{f}}$ across the cell surface. Flux quantities are represented using the upwind biased, flux-difference-splitting approach of Roe[15] with third-order accuracy. Salient aspects of this formulation are included in Appendix 2 and additional details have been given by Vatsa et al[6]. Solutions are advanced in time with a spatially-split, three-factor approximate factorization method in diagonalized form.

Interface quantities between longitudinal blocks are determined in a conservative second-order accurate manner. At the interface between the two blocks, the conserved variables are interpolated across the overlapping mesh area using a technique introduced by

2

Ramshaw[16]. The conservation of mass, momentum, and energy are maintained across the interface boundary by redistributing the fluxes from one side onto the cell faces of the opposite side. A detailed discussion of the patching algorithm is given by Thomas, et al[17].

Surface Definition and Grid

The surface definition for the F/A-18 forebody-LEX geometry was obtained from a detailed CAD description of the 6% scale model tested by Erickson[10]. The configuration was modeled from the nose longitudinally back to $x/\bar{c} = 2.337$, a station slightly ahead of the LEX-wing juncture ($x/\bar{c} = 2.482$) at which point the LEX leading-edge has already achieved 90° of sweep, Fig. 1. A downstream extension of the surface is then obtained by repeating the cross-sectional geometry from this station as described in the following paragraphs.

The grid is divided into two longitudinal blocks which interface along a plane $x = const.$ at the LEX apex station, Fig. 2. The forward block extends upstream of the nose by approximately 1.5 $\bar{c}$ and the aft block extends downstream of the LEX-wing station by approximately 1.5 $\bar{c}$; both blocks extend radially from the model centerline by approximately 2.4 $\bar{c}$. (For the downstream extension, the model cross-section is held constant.) The reference length $\bar{c}$ is comparable to the longitudinal extent of the forebody and 3/4 of the longitudinal extent of the LEX-body juncture.

The three-dimensional grid for each block is constructed from two-dimensional O-type cross flow grids which are longitudinally stacked, constituting an H-O topology. Both blocks have 65 points in the radial direction; the upstream block has 31 points circumferentially whereas the downstream block has an additional 34 points in the circumferential direction to represent the LEX. A more detailed view of the discrete surface representation is shown in Fig. 3(a). With the blocked approach, the LEX apex is represented as a singular point while the body representation is continuous through this station. Longitudinally, the grid is clustered near the nose and LEX-apex regions with 17 stations on the forebody and 22 stations on the LEX-body. The grid is completed with 10 stations extending upstream from the nose and 9 stations extending downstream from the station $x/\bar{c} = 2.337$; both extensions incorporate longitudinal stretching to provide resolution near the configuration. (The grid upstream of the nose was treated as a separate block for turbulent flow computations). The F/A-18 forebody-LEX surface geometry is represented with a total of 1,957 points, and the entire grid consists of approximately 185,000 points.

The crossflow grids are generated using established transfinite interpolation techniques[18,19] with a method applicable to slender shapes[20]. A baseline grid (of approximately 185,000 points) is first established with sufficient normal clustering near the surface to adequately resolve the laminar sublayer for the turbulent boundary layer flow at the subject wind-tunnel freestream conditions ($M_\infty = 0.6$, $R_{\bar{c}} = 0.8 \times 10^6$, and $\alpha = 20°$). This grid produced an average normal cell size next to the wall of approximately $10^{-4}\bar{c}$ which corresponds to $y^+ \approx 2$ for the turbulent computations; a laminar sublayer generally extends out to $y^+ \approx 8.5$. The same grid is used for the laminar computations as well. Fig. 3(b) illustrates the nearfield grid structure about a typical F/A-18 LEX-body cross section. This figure illustrates the challenge that is associated with generating a single O-type grid around such complex cross section with various break points in the surface geometry. Additional details of the grid resolution in the LEX-body juncture as well as the LEX leading-edge regions are shown in Fig. 3(c) and Fig. 3(d), respectively.

At the subject flight freestream conditions ($M_\infty = 0.34$, $R_{\bar{c}} = 13.5 \times 10^6$, and $\alpha = 19°$) the baseline grid produced $y^+ \approx 8$. Although an average y^+ slightly less than 10 has been reported[8] to provide adequate viscous resolution, a grid sensitivity investigation was conducted to provide solutions at flight conditions with comparable viscous resolution to those already achieved at wind-tunnel conditions. The baseline grid was modified to have twice the number of points in the normal direction with increased clustering such that approximately 4.5 fine grid cells were packed in the first cell of the baseline grid. The longitudinal and circumferential grid distributions were not altered. The resultant fine grid consists of approximately 370,000 points and yields $y^+ \approx 3$ for the turbulent computations at flight conditions.

Results and Discussion

All computations were performed on the NAS Cray 2, located at NASA-Ames. On this machine, the algorithm requires approximately 22 μ seconds per grid point per cycle. Converged results were obtained in nominally 2200 cycles requiring about 2.5 hours of computer time for the baseline grid. This number of cycles was sufficient to reduce the residuals by two to three orders of magnitude and to reduce oscillations in C_L and C_D to a negligible level. The computations were performed without the use of mesh sequencing or multigrid iteration.

Results are presented for the subject wind-tunnel and flight test conditions. All comparisons of computed results (e.g. laminar vs. turbulent, baseline vs. refined grid, etc.) within a figure are presented from an identical vantage point. The magnitudes associated with contour quantities are displayed with a color bar.

Wind-Tunnel Computations

The computed total pressure contours and surface streamline patterns are shown in Fig. 4 for both laminar as well as turbulent flow calculations. These solutions are obtained at $M_\infty = 0.6$, $R_{\bar{c}} = 0.8 \times 10^6$, and $\alpha = 20°$. The cross flow total pressure contours for the laminar computations (Fig. 4(a)) clearly show the LEX primary and the secondary vortex systems. In addition, the same crossflow contours show an appreciable body type separation under the LEX which will be discussed later in detail. Furthermore, there exists a clear primary separation line (as indicated by the converging surface streamlines) on the forebody along with a secondary separation line on the leeward side of the aft forebody. These are fairly flat bubble-type separations which, in general, occur on the order of a boundary layer thickness. The primary and the secondary separation lines merge and wrap around the LEX apex with a subsequent entrainment into the juncture between the LEX upper surface and the body. The turbulent flow computations demonstrate a drastically different flow structure as shown in Fig. 4(b). For example, it appears that the primary and the secondary forebody separations are completely eliminated in the turbulent case. Additional differences are discussed subsequently.

A closeup view of the LEX-body flow structure is shown in Fig. 5 for both laminar and turbulent flow. These results clearly show the very complex flow that exists under the LEX, especially for the laminar flow solution (Fig. 5(a)). It appears that for this result, there is a bubble type separation under the LEX apex, similar to what occurred on the forebody. Further downstream a larger vortex-like separation is evident along with secondary separation effects. Once again there are significant differences between laminar and turbulent computations as shown in Fig. 5(b). The body separation under the LEX is changed considerably by occurring closer to the LEX lower surface and practically filling up the entire corner region. The separation pattern for the turbulent case is much simpler than the corresponding pattern for the laminar case.

Fig. 5 also provides a close view of the surface flow in the vicinity of the longitudinal grid-patching station (i.e., the LEX apex station). Note that the flow properties are very smooth across this interfacing patch between the two blocks of grid.

The LEX upper surface flow pattern computed at the wind tunnel flow conditions for both laminar and turbulent flow are shown in Fig. 6. The laminar computation (Fig. 6(a)) clearly shows the secondary separation line with the subsequent reattachment line (indicated by the diverging surface streamlines) between the primary separation line and the leading edge. A

tertiary separation is also indicated outboard of the secondary separation line. The turbulent computation (Fig. 6(b)) show the outboard movement of the secondary separation line, as expected, and reduced evidence of the tertiary flow.

The normalized density contours at various LEX crossflow planes are shown in Fig. 7 for laminar and turbulent flow. The color bar in the upper right corner of the figure indicate the level of compressibility associated with the core of the LEX vortex system. In the vortex core region there is a 40% to 50% expansion compared to the freestream condition. Note that the laminar and turbulent computations produced very similar density contours. Additional analysis indicated that the majority of the core flow achieved a local Mach number of 0.9 or greater with a small supersonic zone occurring near the LEX apex.

Contours of the static surface pressure coefficient are shown in Fig. 8 for both laminar and turbulent flow computations. The results show a compression region around the apex of the LEX as well as the foot print of low pressure associated with the LEX primary and secondary vortices on the LEX surface. Although these surface contours of the laminar and turbulent solutions look very similar, a more detailed assessment indicates significant differences as will be discussed subsequently in conjunction with experimental wind tunnel data. The experimental stations are highlighted in white and are located at $x/\bar{c} = 0.334, 0.587, 0.891, 1.390, 1.701$, and 2.143. For reference, the LEX apex is located at $x/\bar{c} = 1.006$ and the LEX-wing juncture at $x/\bar{c} = 2.482$.

The comparison of the computed surface pressure coefficients for both laminar and turbulent flow are shown in Fig. 9 at the six different stations. The experimental data are also shown for both the starboard and port sides of the model to assess flow symmetry. Figures 9(a)-(c) show the variation of the surface pressure coefficients as a function of azimuthal angle θ on the forebody. The windward and leeward sides of the forebody correspond to $\theta = 0°$ and $180°$, respectively. Both laminar and turbulent solutions slightly underpredict the pressure peak at station 1 as shown in Fig. 9(a). This underprediction of the pressure peak could well be attributed to the inability of the H-O grid topology to resolve the flow near forebody nose. This figure also indicates the differences between the laminar and turbulent solutions which occur in the range $130° \leq \theta \leq 165°$. This difference is due to the separated zones on the forebody which occur for laminar flow. Figures 9(b)-(c) show a very good correlation between the computational results and the experimental data, particularly the turbulent flow solution. The differences between theory and experiment shown in

Fig. 9(c) near $\theta = 0°$ and $\theta = 180°$ are believed to be associated with circumferential grid resolution.

The LEX computed surface pressure coefficients are shown in Fig. 9(d)-(f) along with the experimental data as a function of LEX exposed semispan, y/s. In this way, $y/s = 0$ corresponds to the LEX-body juncture and $y/s = 1$ corresponds to the LEX leading edge. Figure 9(d) reveals a good agreement between the experimental data and the turbulent flow computation. This figure also shows that the laminar flow under predicts the low pressure peak that is associated with the primary vortex system. This difference between the laminar and turbulent solutions was not as evident on the color surface pressure contours shown earlier in Fig. 8. The correlation between theory and experiment begins to degrade at station 5, Fig. 9(e), and continues to do so at station 6, Fig. 9(f). It is believed that this difference is primarily associated with wing-induced up-wash effects present in the experimental data. The test was conducted with a complete F/A-18 configuration, including flow-through inlets, whereas the computations only modeled the forebody-LEX portion of the configuration. The wing-induced effects would be strongest near the aft portion of the LEX and, in general, would cause more negative suction pressures by strengthening the LEX vortex. Inlet-induced effects are a secondary source for this discrepancy. None the less, it is noteworthy that the forebody pressures as well as the pressures on the forward portion of the LEX can be accurately predicted with the turbulent computations on the isolated forebody-LEX geometry.

The correlation between theory and experiment is *further assessed by examining the experimental sensitivity* of the surface pressures to changes in angle of attack as well as Mach number, Fig. 10. In this figure results are presented for stations 3 and 4 which represent experimental perturbations about the subject wind-tunnel conditions; the turbulent theory from the prior figure is also included. The data are shown to be quite sensitive to changes in angle of attack of $\pm 2.5°$ as well as to changes in freestream Mach number from 0.4 to 0.7. The differences between theory and experiment are, in general, significantly less than the the incremental effects of α and M_∞ shown in the experiment.

Flight-Test Computations

The flight-test solutions are obtained at $M_\infty = 0.34$, $R_{\bar{c}} = 13.5 \times 10^6$, and $\alpha = 19°$. Due to the high Reynolds number associated with flight, grid sensitivity effects were assessed. Various flow parameters (e.g., Mach contours, density contours, surface flow patterns, surface pressure contours, etc.) were contrasted between the solutions obtained with either the baseline

or the refined grid. No major differences between these solutions were found. Typical results which contrast the baseline and refined grid solutions are presented in Fig. 11 for static surface pressure contours and in Fig. 12 for the LEX upper-surface flow pattern. It was concluded from this study that the baseline grid provided credible solutions which could be used for the subsequent correlations with the flight test results.

The total pressure contours at various crossflow stations as well as the surface flow pattern computed at flight condition are shown in Fig. 13. Fig. 13(a) shows an overall view of the flow, whereas Fig. 13(b) illustrates the LEX-body flow details. The forebody surface flow pattern qualitatively resembles the turbulent solution obtained at wind tunnel flow conditions (c.f., Fig. 4(b)) in that the flow appears to remain attached. The LEX-body flow exhibits greater differences between flight (Fig. 13(b)) and wind-tunnel (Fig. 5(b)) conditions principally with respect to the body separation under the LEX. This separated zone is smaller at the flight conditions than was observed in the wind-tunnel computations.

A side view of the computed surface flow stream-lines on the forebody at flight condition is shown in Fig. 14(a). This figure also shows part of the LEX geometry. The surface flow pattern obtained in flight is shown in Fig. 14(b) from a similar vantage point. The body separation line under the LEX is well predicted by the theory. Furthermore, the overall surface flow pattern around the forebody agree well, qualitatively, with the flight test results. Similarly, Fig. 15 show a correlation between the computed surface streamlines and the flight test results on the windward side (of the front part) of the forebody. The correlation between these results is also quite good.

Concluding Remarks

Three dimensional viscous flow computations for the F/A-18 forebody-LEX are presented for both wind tunnel as well as flight conditions. At wind tunnel condition, significant difference between laminar and turbulent solutions are revealed, particularly on the surface flow pattern. Good agreement between the computed surface pressure coefficient and the experimental data are also disclosed. The turbulent computations provided a better correlation with the data. At flight condition, the grid sensitivity study revealed that the baseline grid clustering with only 185,000 points was sufficient to adequately resolve the viscous laminar-sublayer for the turbulent computations. Furthermore, the computed surface flow pattern correlated well, qualitatively, with the flight test results.

Appendix 1 - Governing Equations

The inviscid flux terms from the governing equation are defined as follows:

$$\hat{Q} = \frac{1}{J}\begin{Bmatrix} \rho \\ \rho u \\ \rho v \\ \rho w \\ E \end{Bmatrix} \quad ; \quad \hat{F} = \frac{1}{J}\begin{Bmatrix} \rho U \\ \rho U u + \xi_{,x}p \\ \rho U v + \xi_{,y}p \\ \rho U w + \xi_{,z}p \\ (E+p)U \end{Bmatrix}$$

$$\hat{G} = \frac{1}{J}\begin{Bmatrix} \rho V \\ \rho V u + \eta_{,x}p \\ \rho V v + \eta_{,y}p \\ \rho V w + \eta_{,z}p \\ (E+p)V \end{Bmatrix} \quad ; \quad \hat{H} = \frac{1}{J}\begin{Bmatrix} \rho W \\ \rho W u + \varsigma_{,x}p \\ \rho W v + \varsigma_{,y}p \\ \rho W w + \varsigma_{,z}p \\ (E+p)W \end{Bmatrix}$$

The contravariant velocity components in these equations are given by:

$$\begin{Bmatrix} U \\ V \\ W \end{Bmatrix} = \begin{Bmatrix} \xi_{,x}u + \xi_{,y}v + \xi_{,z}w \\ \eta_{,x}u + \eta_{,y}v + \eta_{,z}w \\ \varsigma_{,x}u + \varsigma_{,y}v + \varsigma_{,z}w \end{Bmatrix}$$

The viscous flux terms from the governing equation are defined as follows:

$$\hat{F}_v = \frac{M_\infty \mu}{R_eJ}\begin{Bmatrix} 0 \\ u_{,\xi}\phi_{\xi1} + \xi_{,x}\phi_{\xi2} \\ v_{,\xi}\phi_{\xi1} + \xi_{,y}\phi_{\xi2} \\ w_{,\xi}\phi_{\xi1} + \xi_{,z}\phi_{\xi2} \\ ((\frac{q^2}{2})_{,\xi} + \frac{T_{,\xi}}{Pr(\gamma-1)})\phi_{\xi1} + U\phi_{\xi2} \end{Bmatrix}$$

$$\hat{G}_v = \frac{M_\infty \mu}{R_eJ}\begin{Bmatrix} 0 \\ u_{,\eta}\phi_{\eta1} + \eta_{,x}\phi_{\eta2} \\ v_{,\eta}\phi_{\eta1} + \eta_{,y}\phi_{\eta2} \\ w_{,\eta}\phi_{\eta1} + \eta_{,z}\phi_{\eta2} \\ ((\frac{q^2}{2})_{,\eta} + \frac{T_{,\eta}}{Pr(\gamma-1)})\phi_{\eta1} + V\phi_{\eta2} \end{Bmatrix}$$

$$\hat{H}_v = \frac{M_\infty \mu}{R_eJ}\begin{Bmatrix} 0 \\ u_{,\varsigma}\phi_{\varsigma1} + \varsigma_{,x}\phi_{\varsigma2} \\ v_{,\varsigma}\phi_{\varsigma1} + \varsigma_{,y}\phi_{\varsigma2} \\ w_{,\varsigma}\phi_{\varsigma1} + \varsigma_{,z}\phi_{\varsigma2} \\ ((\frac{q^2}{2})_{,\varsigma} + \frac{T_{,\varsigma}}{Pr(\gamma-1)})\phi_{\varsigma1} + W\phi_{\varsigma2} \end{Bmatrix}$$

where

$$\begin{Bmatrix} \phi_{\xi1} \\ \phi_{\eta1} \\ \phi_{\varsigma1} \end{Bmatrix} = \begin{Bmatrix} (\xi_{,x})^2 + (\xi_{,y})^2 + (\xi_{,z})^2 \\ (\eta_{,x})^2 + (\eta_{,y})^2 + (\eta_{,z})^2 \\ (\varsigma_{,x})^2 + (\varsigma_{,y})^2 + (\varsigma_{,z})^2 \end{Bmatrix}$$

$$\begin{Bmatrix} \phi_{\xi2} \\ \phi_{\eta2} \\ \phi_{\varsigma2} \end{Bmatrix} = \frac{1}{3}\begin{Bmatrix} u_{,\xi}\xi_{,x} + v_{,\xi}\xi_{,y} + w_{,\xi}\xi_{,z} \\ u_{,\eta}\eta_{,x} + v_{,\eta}\eta_{,y} + w_{,\eta}\eta_{,z} \\ u_{,\varsigma}\varsigma_{,x} + v_{,\varsigma}\varsigma_{,y} + w_{,\varsigma}\varsigma_{,z} \end{Bmatrix}$$

The transformation metrics are:

$$\begin{bmatrix} \xi_{,x} & \eta_{,x} & \varsigma_{,x} \\ \xi_{,y} & \eta_{,y} & \varsigma_{,y} \\ \xi_{,z} & \eta_{,z} & \varsigma_{,z} \end{bmatrix} =$$

$$J\begin{bmatrix} y_{,\eta}z_{,\varsigma} - z_{,\eta}y_{,\varsigma} & z_{,\xi}y_{,\varsigma} - y_{,\xi}z_{,\varsigma} & y_{,\xi}z_{,\eta} - z_{,\xi}y_{,\eta} \\ z_{,\eta}x_{,\varsigma} - x_{,\eta}z_{,\varsigma} & x_{,\xi}z_{,\varsigma} - z_{,\xi}x_{,\varsigma} & z_{,\xi}x_{,\eta} - x_{,\xi}z_{,\eta} \\ x_{,\eta}y_{,\varsigma} - y_{,\eta}x_{,\varsigma} & y_{,\xi}x_{,\varsigma} - x_{,\xi}y_{,\varsigma} & x_{,\xi}y_{,\eta} - y_{,\xi}x_{,\eta} \end{bmatrix}$$

and the Jacobian of the transformation is given by:

$$J^{-1} = x_{,\xi}(y_{,\eta}z_{,\varsigma} - z_{,\eta}y_{,\varsigma}) - y_{,\xi}(x_{,\eta}z_{,\varsigma} - z_{,\eta}x_{,\varsigma})$$
$$+ z_{,\xi}(x_{,\eta}y_{,\varsigma} - y_{,\eta}x_{,\varsigma})$$

Appendix 2 - Upwind Algorithm

Spatial derivatives are expressed as a conservative flux balance across a cell such as

$$(\delta\hat{F}/\delta\xi)_i = (\hat{F}_{i+1/2} - \hat{F}_{i-1/2})/(\xi_{i+1/2} - \xi_{i-1/2})$$

and the interface flux is expressed as

$$\hat{F}_{i+1/2} = \frac{1}{2}[\hat{F}(Q_L) + \hat{F}(Q_R) - |\tilde{A}|(Q_R - Q_L)]_{i+1/2}$$

Here Q_L and Q_R are the state variables in the left and right cells and

$$A \equiv \partial\hat{F}/\partial Q = T(\Lambda^+ + \Lambda^-)T^{-1}$$

T and T^{-1} are diagonalizing matrices and Λ is the diagonal matrix of eigenvalues with

$$\Lambda^\pm = \frac{1}{2}(\Lambda \pm |\Lambda|) \quad ; \quad |A| = T|\Lambda|T^{-1}$$

The superscript $\tilde{}$ denotes evaluation of the matrices with Roe-averaged quantities such as

$$\tilde{\rho} = \sqrt{\rho_L\rho_R}$$

$$\tilde{u} = (u_L + u_R\sqrt{\rho_R/\rho_L})/(1 + \sqrt{\rho_R/\rho_L})$$

$$\tilde{v} = (v_L + v_R\sqrt{\rho_R/\rho_L})/(1 + \sqrt{\rho_R/\rho_L})$$

$$\tilde{w} = (w_L + w_R\sqrt{\rho_R/\rho_L})/(1 + \sqrt{\rho_R/\rho_L})$$

$$\tilde{H} = (H_L + H_R\sqrt{\rho_R/\rho_L})/(1 + \sqrt{\rho_R/\rho_L})$$

$$\tilde{a}^2 = (\gamma - 1)(\tilde{H} - (\tilde{u}^2 + \tilde{v}^2 + \tilde{w}^2)/2)$$

so that

$$\hat{F}(Q_R) - \hat{F}(Q_L) = \tilde{A}[Q_R - Q_L]$$

is satisfied exactly.

State variables at the cell interfaces are formed from interpolation of the primitive variables $q \equiv [\rho, u, v, w, p]^T$ by the one-parameter family

$$(q_L)_{i+1/2} = q_i + \frac{1}{4}[(1-\kappa)\overline{\nabla q_i} + (1+\kappa)\overline{\triangle q_i}]$$

$$(q_R)_{i+1/2} = q_{i+1} - \frac{1}{4}[(1+\kappa)\overline{\nabla q_{i+1}} + (1-\kappa)\overline{\triangle q_{i+1}}]$$

where the backward and forward differences are expressed respectively with a typical *minmod* limiter as

$$\overline{\nabla q} = minmod[\nabla q, B \triangle q]$$

$$\overline{\triangle q} = minmod[\triangle q, B \nabla q]$$

with

$$minmod(x, y) \equiv sign(x) \times$$
$$max\left[0, min(x \; sign(y), y \; sign(x))\right]$$

Here B is a compression parameter

$$B \equiv (3 - \kappa)/(1 - \kappa)$$

and $\kappa = 1/3$ for third-order accuracy.

Acknowledgments

References

[1] Thomas, J. L.; and Newsome, R. W.: Navier-Stokes Computations of Lee-Side Flows over Delta Wings. AIAA Paper No. 86-1049, 1986.

[2] Vatsa, V. N.: Accurate Solutions for Transonic Viscous Flow Over Finite Wings. AIAA Paper No. 86-1052, 1986.

[3] Thomas, J. L.; Taylor, S. L.; and Anderson, W. K.: Navier-Stokes Computations of Vortical Flows Over Low Aspect Ratio Wings. AIAA Paper No. 87-0207, 1987.

[4] Newsome, R. W.; and Adams, M. S.: Numerical Simulation of Vortical-Flow Over an Elliptical-Body Missile at High Angles of Attack. AIAA Paper No. 86-0559, 1986.

[5] Ying, S. X.; Steger, J. L.; Schiff, L. B.; and Bagdanoff, D.: Numerical Simulation of Unsteady, Viscous, High Angle of Attack Flows Using a Partially Flux-Split Algorithm. AIAA Paper No. 86-2179, 1986.

[6] Vatsa, V. N.; Thomas, J. L., and Wedan, B. W.: Navier-Stokes Computations of Prolate Spheroids at Angle of Attack. AIAA Paper No. 87-2627-CP, 1987.

[7] Walters, R. W.; Reu, T.; McGrory, W. D.; Thomas, J. L.; and Richardson, P. F.: A Longitudinally-Patched Grid Approach with Applications to High Speed Flows. AIAA Paper No. 88-0715, 1988.

[8] Flores, J.; and Chaderjian, N. M.: The Numerical Simulation of Transonic Separated Flow About the Complete F-16A. AIAA Paper No. 88-2506, 1988.

[9] Buning, P. G.; Chiu, I. T.; Obayashi, S.; Rizk, Y. M.; and Steger, J. L.: Numerical Simulation of the Integrated Space Shuttle Vehicle in Ascent. AIAA Paper No. 88-4359, 1988.

[10] Erickson, G. E.: Experimental Study of the F/A-18 Vortex Flows at Subsonic and Transonic Speeds Using a Laser Vapor Screen Technique. SAE Paper No. 881421, 1988.

[11] Fisher, D. F.; Richwine, D. M.;and Banks, D. W.: Surface Flow Visualization of Separated Flows on the Forebody of an F-18 Aircraft and Wind-Tunnel Model. NASA TM 100436, 1988.

[12] Baldwin, B. S.; and Lomax, H.: Thin Layer Approximation and Algebraic Model for Separated Turbulent Flows. AIAA Paper No. 78-257, 1978.

[13] Degani, C.; and Schiff, L. B.: Computation of Supersonic Viscous Flows Around Pointed Bodies at Large Incidence. AIAA Paper No. 83-0034, 1983.

[14] Hartwich, P. M.; and Hall, R. M.: Navier-Stokes Solutions for Vortical Flows over a Tangent-Ogive Cylinder. AIAA Paper No. 89-0337, 1989.

[15] Roe, P. L.: Characteristic Based Schemes for the Euler Equations. Annual Review of Fluid Mechanics, 1986, pp. 337-365.

[16] Ramshaw, J. D.: Conservative Rezoning Algorithms for Generalized Two-Dimensional Meshes. Journal of Computational Physics, Vol. 59, 1985, pp. 193-199.

[17] Thomas, J. L.; Walters, R. W.; Ghaffari, F.: Weston, R. P.; and Luckring, J. M.: A Patched Grid Algorithm for Complex Configurations Directed Towards the F-18 Aircraft. AIAA Paper No. 89-0121, 1989.

[18] Eriksson, L. E.: Practical Three-Dimensional Mesh Generation Using Transfinite Interpolation. Journal of Fluid Mechanics, Vol. 148, 1984, pp. 45-78.

[19] Smith, R. E.: Algebraic Grid Generation. Numerical Grid Generation, Elsevier, New York, 1982, pp. 137-168.

[20] Richardson, P. F.; and Morrison, J. H.: Displacement Surface Calculations for a Hypersonic Aircraft. AIAA Paper No. 87-1190, 1987.
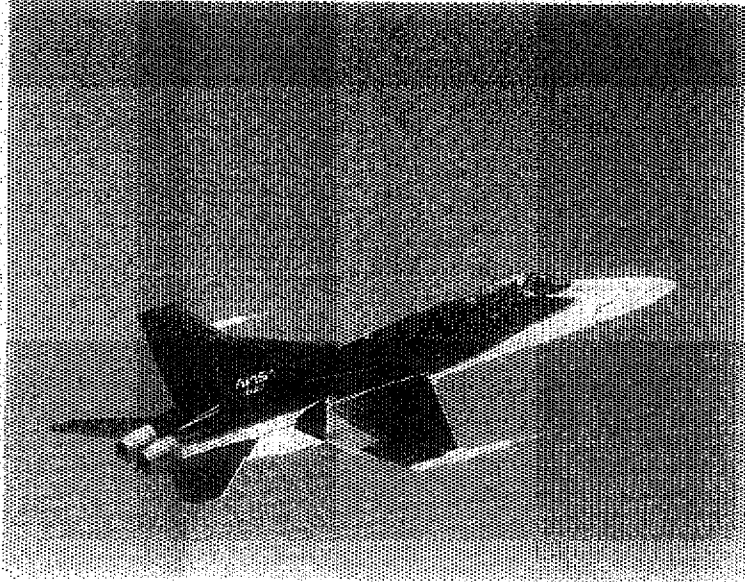
(a) Aircraft.
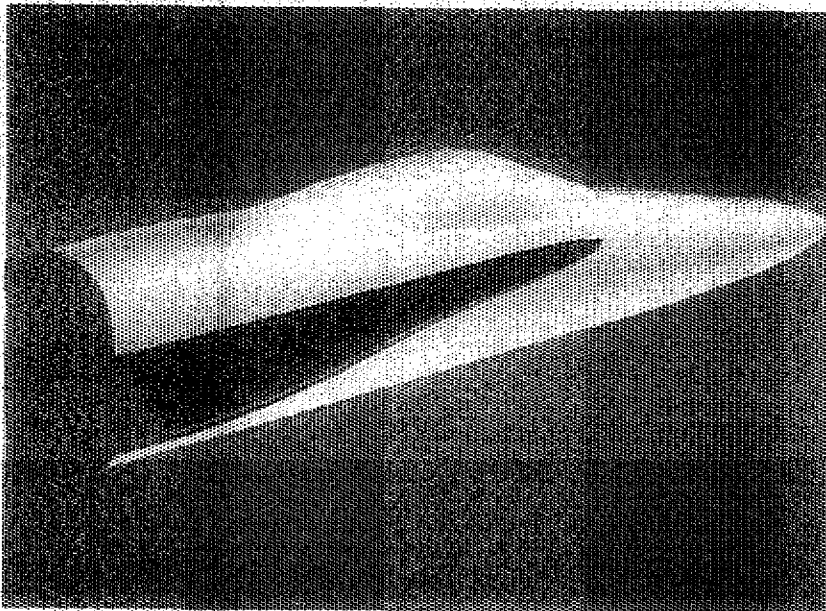
(b) Surface representation.

Figure 1.- F/A-18 HARV vehicle.
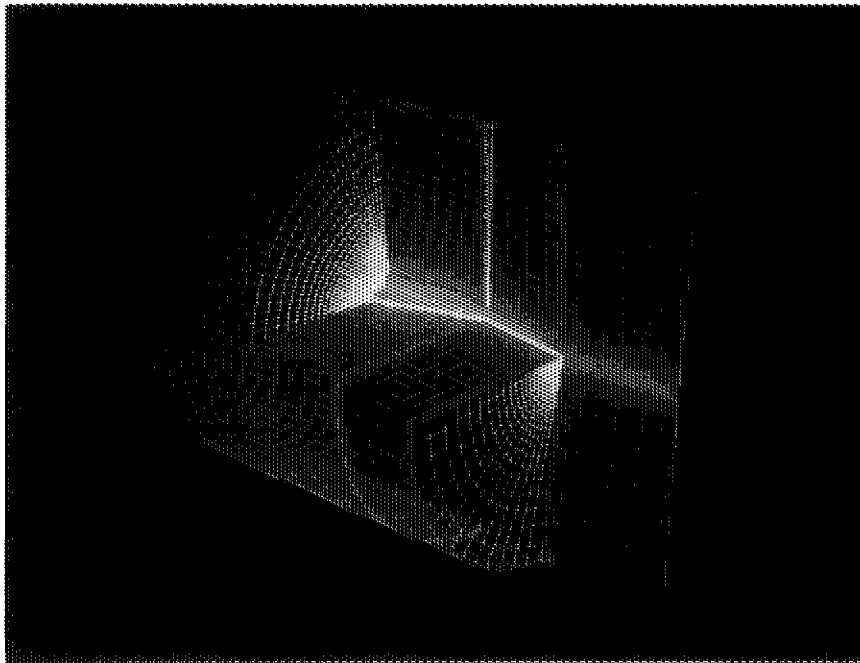
(a) Farfield.
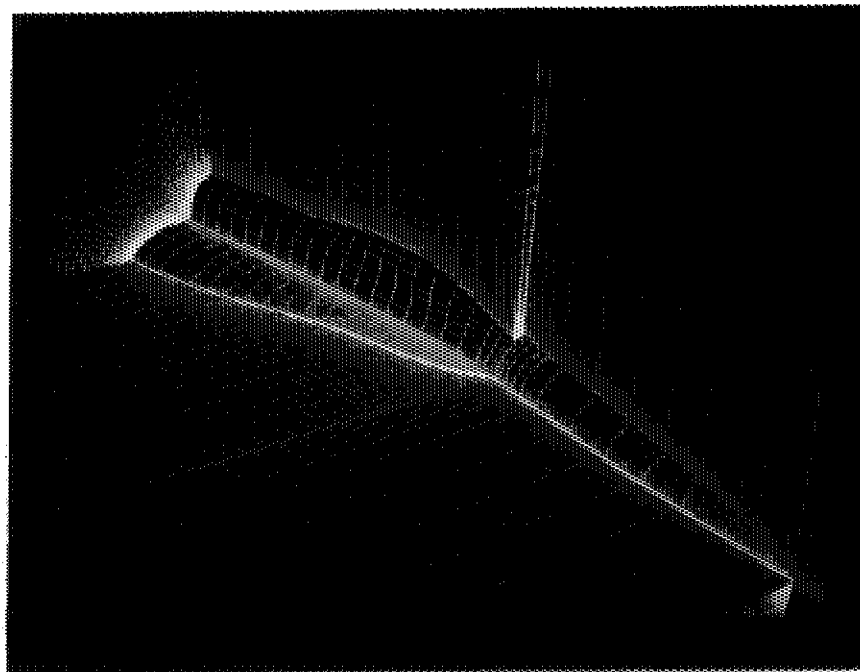
(b) Nearfield.

Figure 2.- Blocking strategy for F/A-18 forebody-LEX grid.
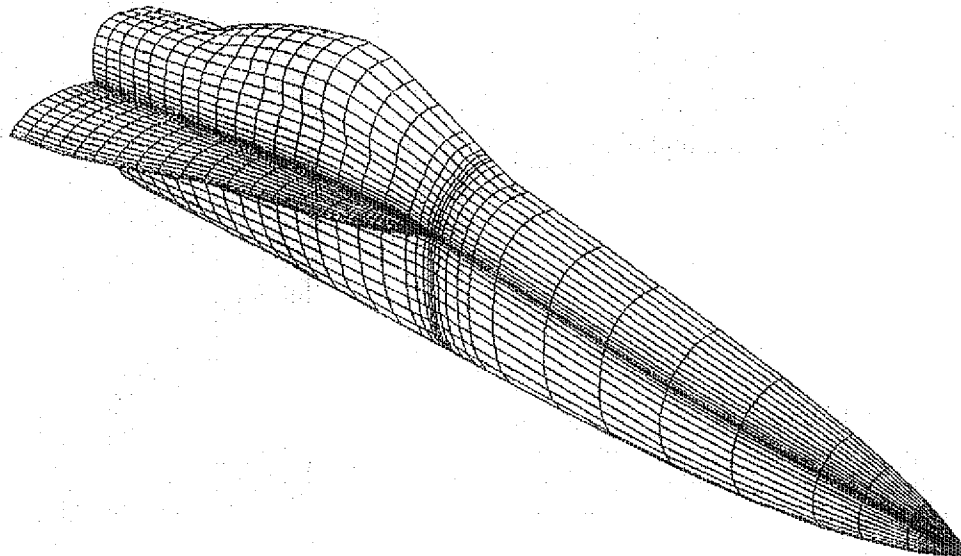
(a) Surface grid.
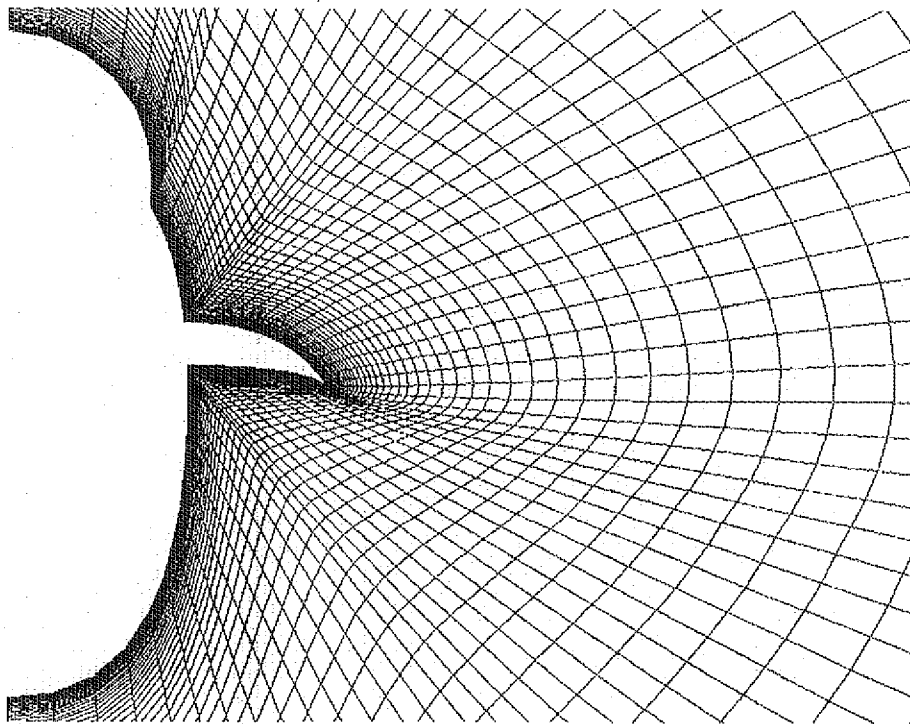
(b) Crossflow plane.

Figure 3.- F/A-18 forebody-LEX grid.
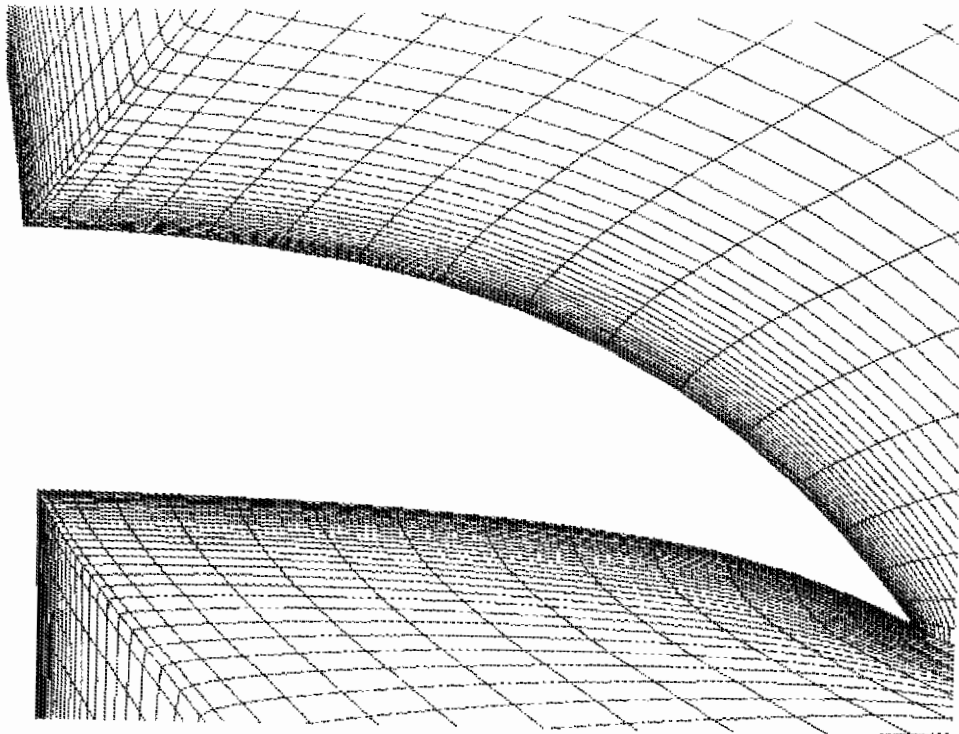
(c) LEX-body detail.
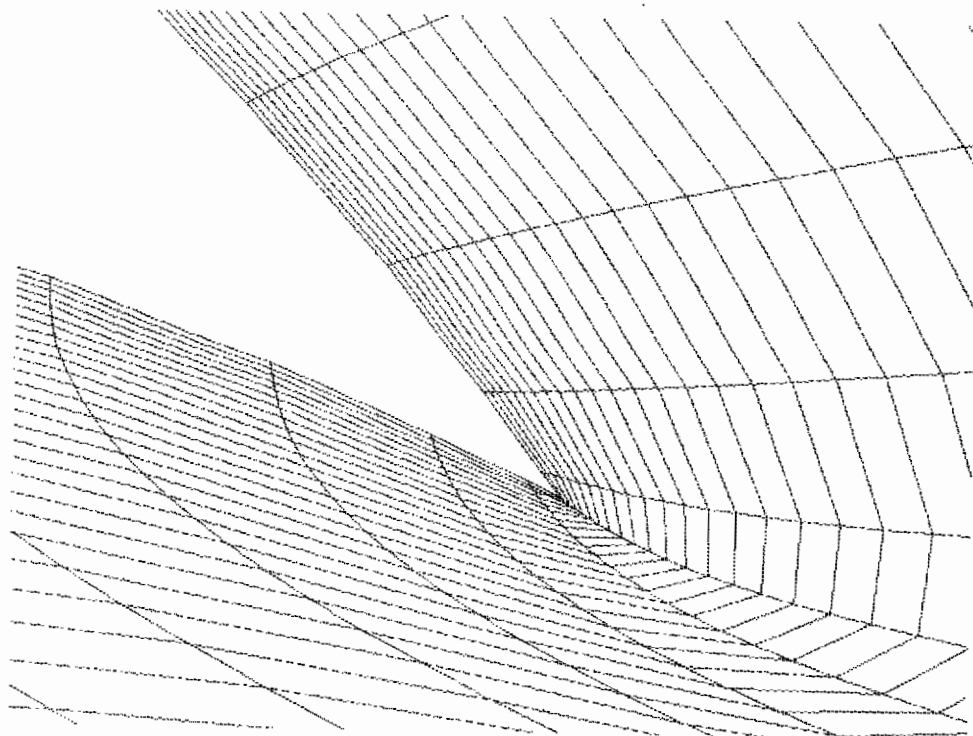
(d)Leading-edge detail.

Figure 3.- F/A-18 forebody-LEX grid - Concluded.
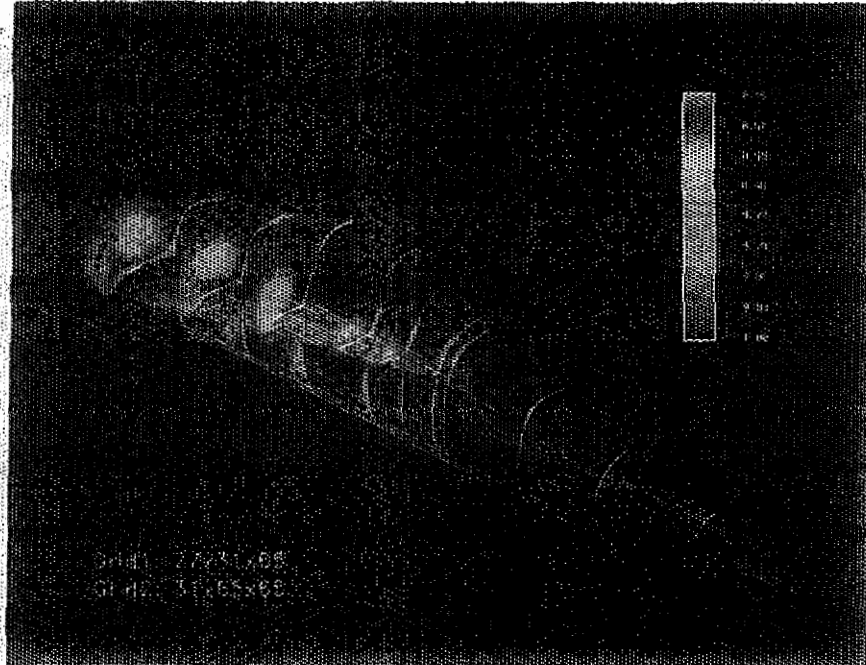
(a) Laminar flow.
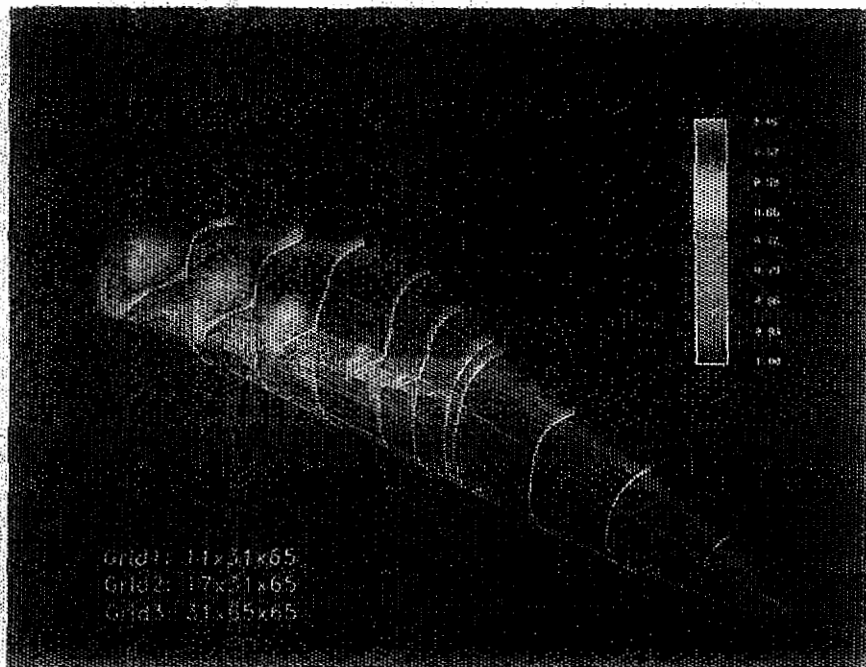
(b) Turbulent flow.

Figure 4.- Total pressure contours with surface flow pattern - overall view. $M_\infty = 0.6, R_c = 0.8 \times 10^6, \alpha = 20^\circ$.
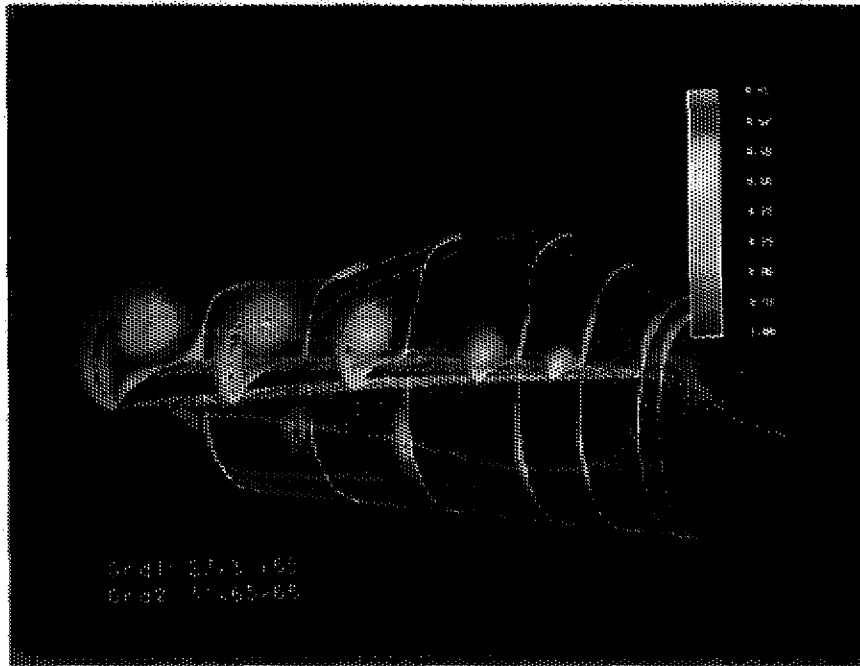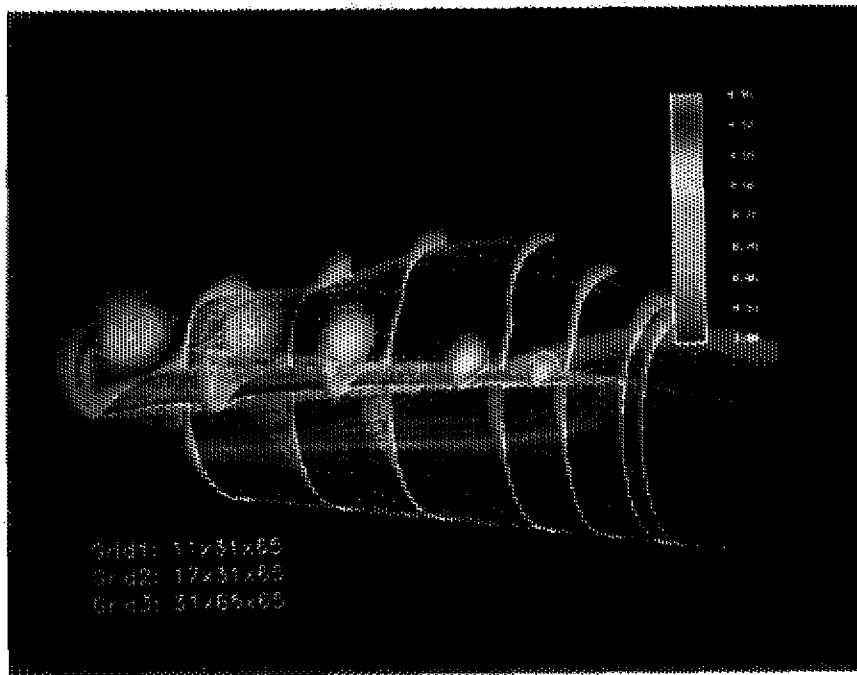
(a) Laminar flow.

(b) Turbulent flow.

Figure 5.- Total pressure contours with surface flow pattern - LEX-body detail. $M_\infty = 0.6$, $R_\ell = 0.8 \times 10^6$, $\alpha = 20°$.
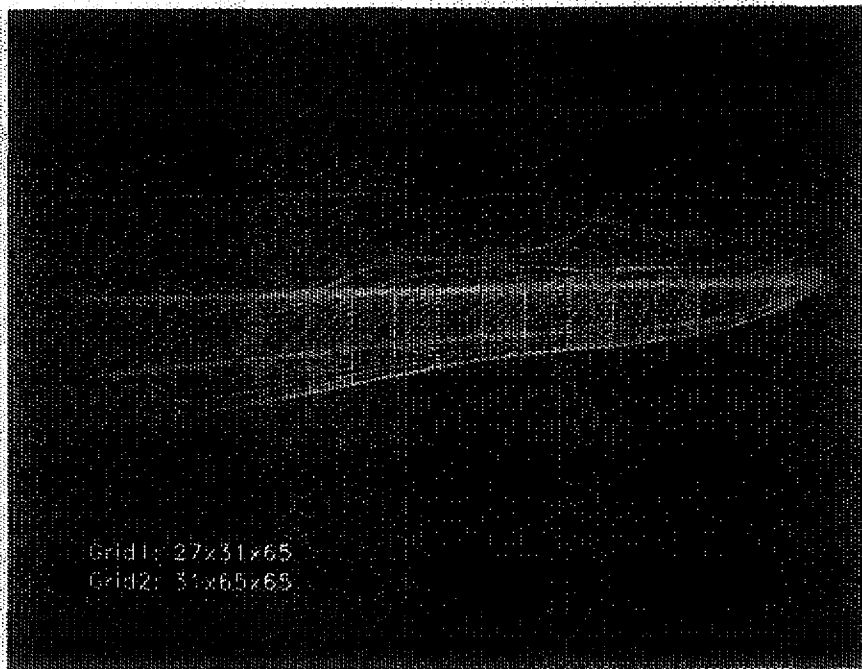
(a) Laminar flow.
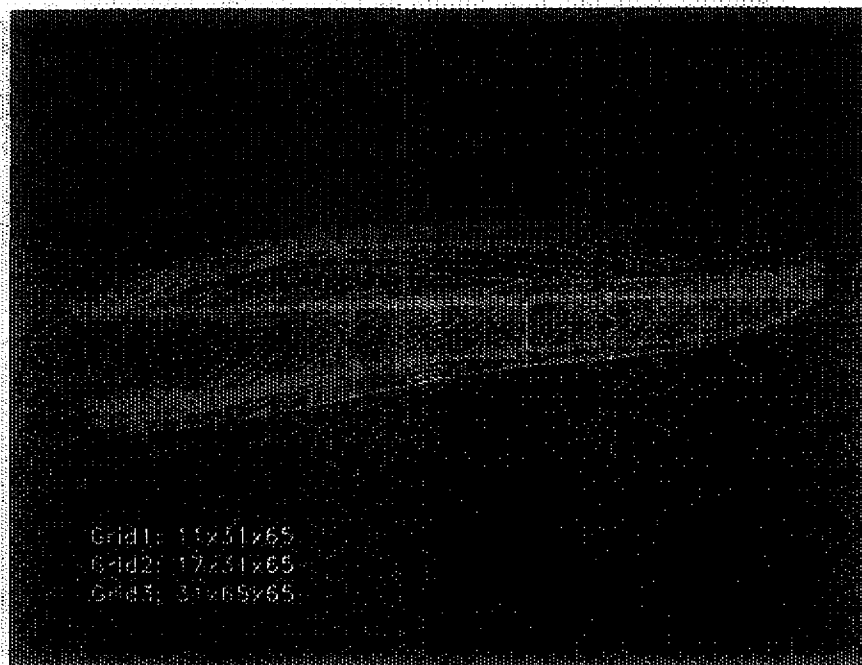
(b) Turbulent flow.

Figure 6.- LEX upper-surface flow pattern. $M_\infty = 0.6, R_c = 0.8 \times 10^6, \alpha = 20^\circ$.
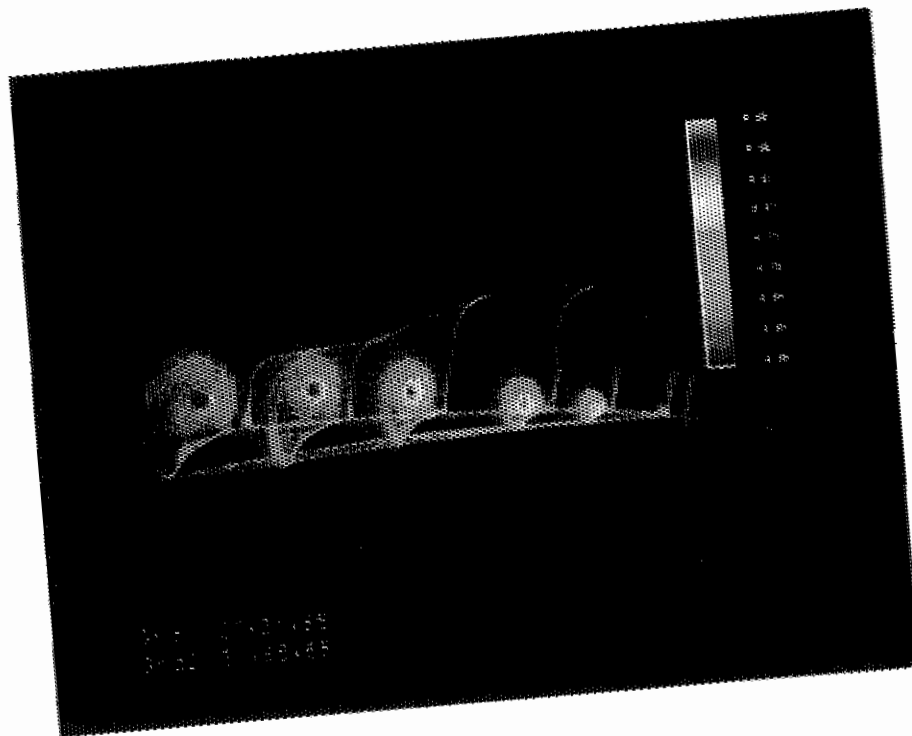
(a) Laminar flow.
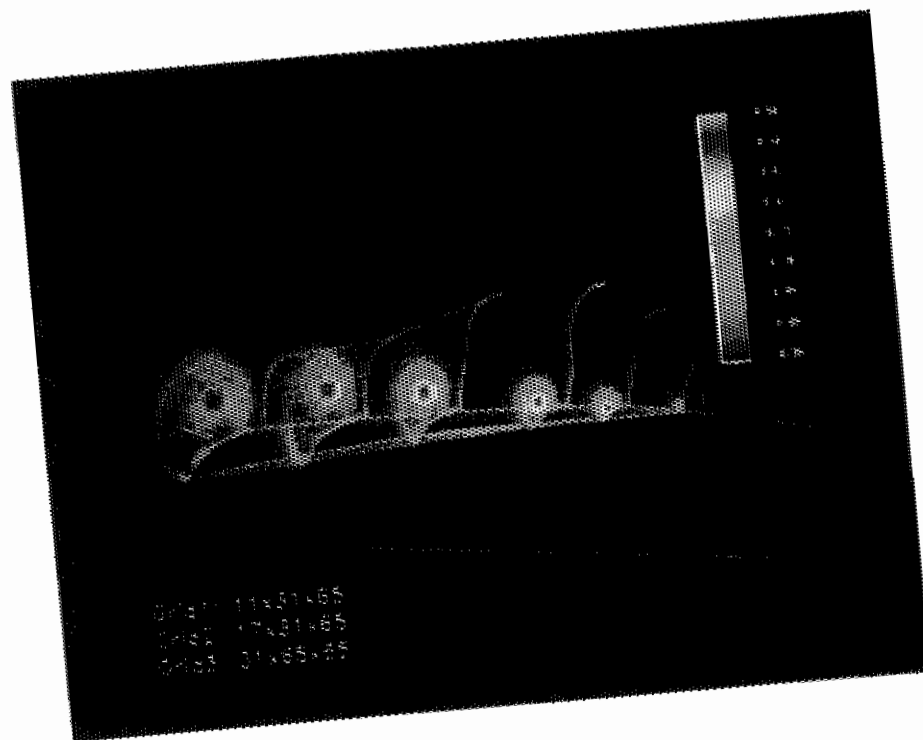
(b) Turbulent flow.

Figure 7.- Density contours in cross-flow planes. $M_\infty = 0.6, R_e = 0.8 \times 10^6, \alpha = 20°$.

15
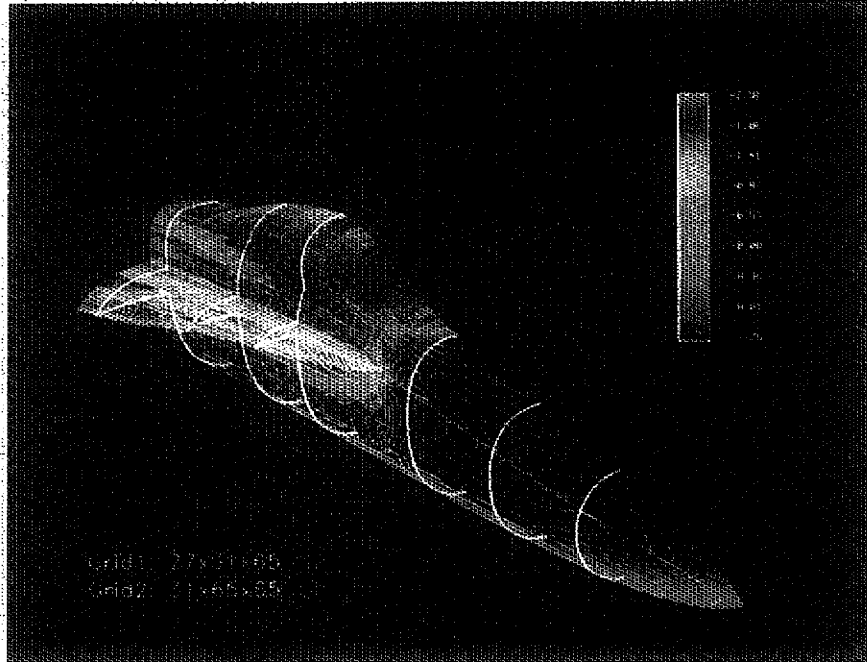
(a) Laminar flow.
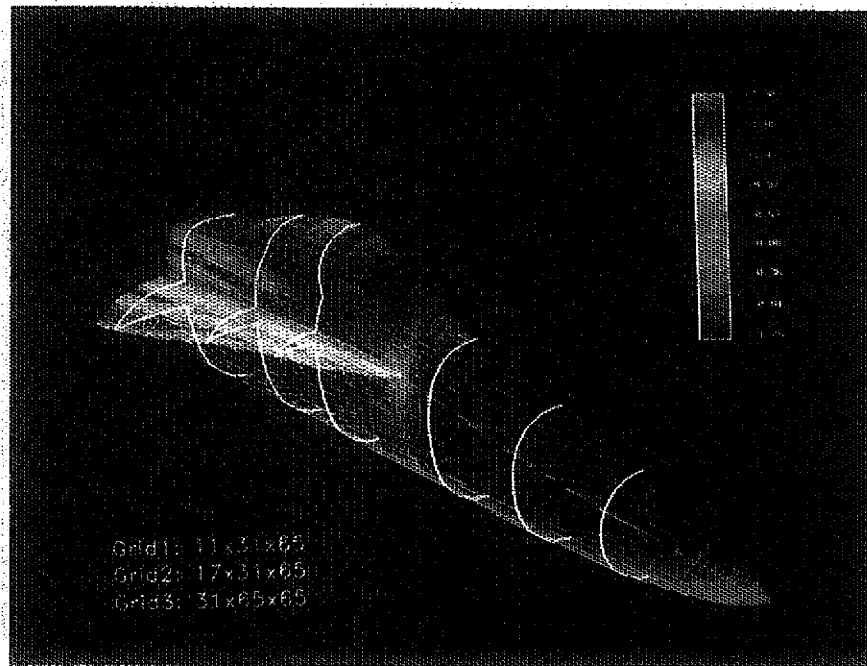
(b) Turbulent flow.

Figure 8.- Static surface pressure coefficient contours. $M_\infty = 0.6, R_c = 0.8 \times 10^6, \alpha = 20^o$.
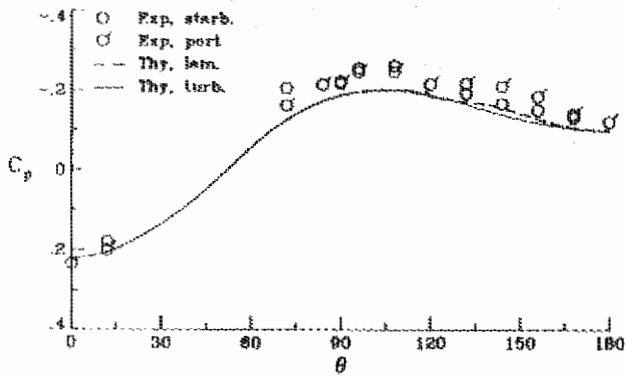
(a) Station 1, $x/\bar{c} = 0.334$.
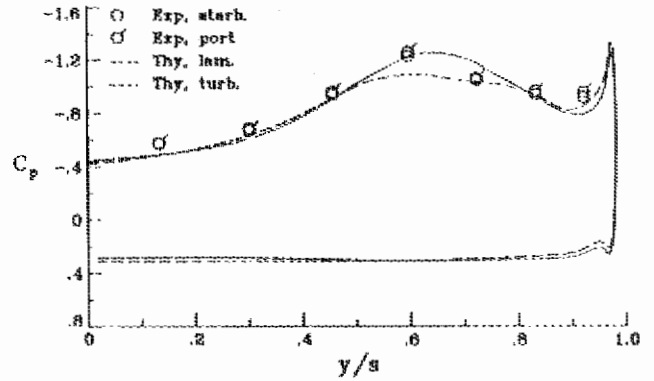
(b) Station 2, $x/\bar{c} = 0.587$.

(c) Station 3, $x/\bar{c} = 0.891$.

(d) Station 4, $x/\bar{c} = 1.390$.
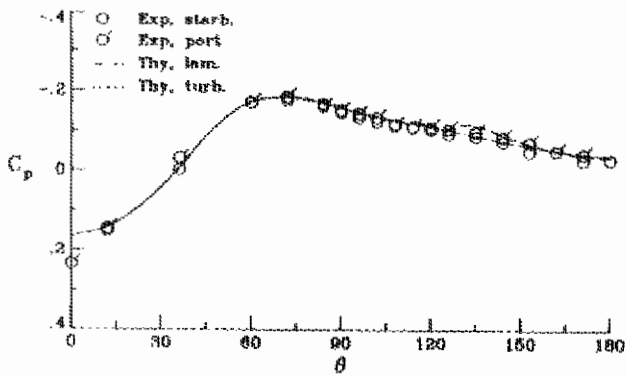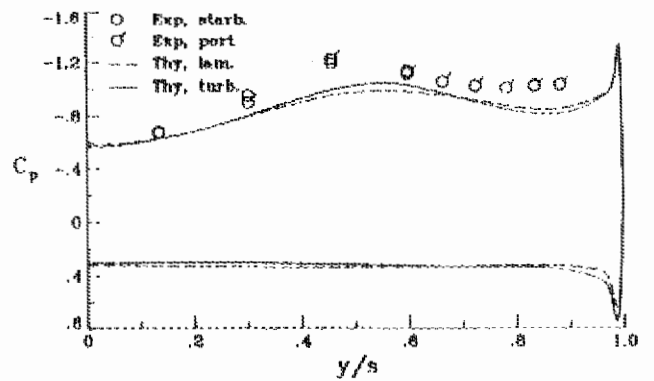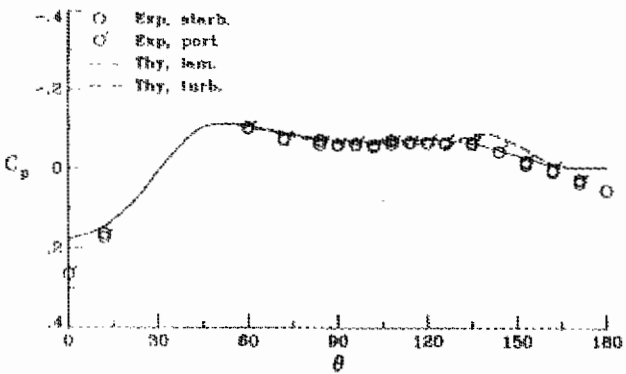
(e) Station 5, $x/\bar{c} = 1.701$.
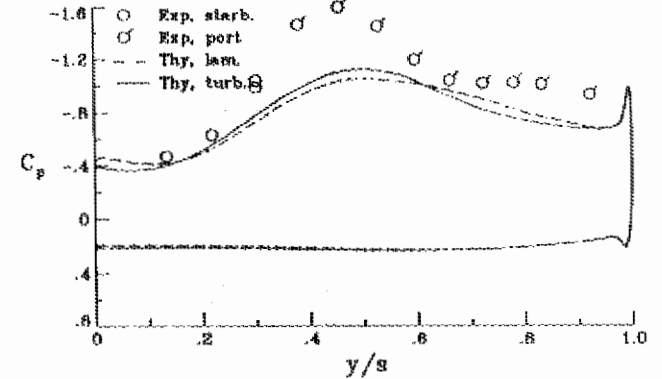
(f) Station 6, $x/\bar{c} = 2.143$.

Figure 9.- Correlation between theory and experiment - surface C_p. $M_\infty = 0.6, R_c = 0.8 \times 10^6, \alpha = 20°$.
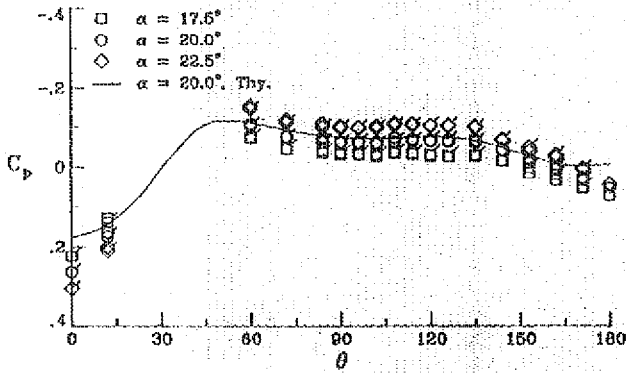
(a) Station 3, $M_\infty = 0.6$.
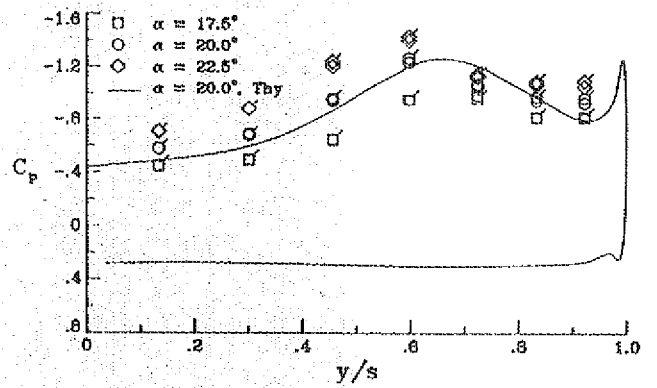
(c) Station 4, $M_\infty = 0.6$.
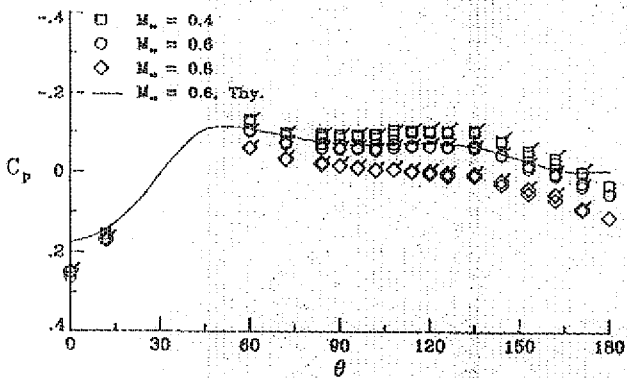
(b) Station 3, $\alpha = 20°$.
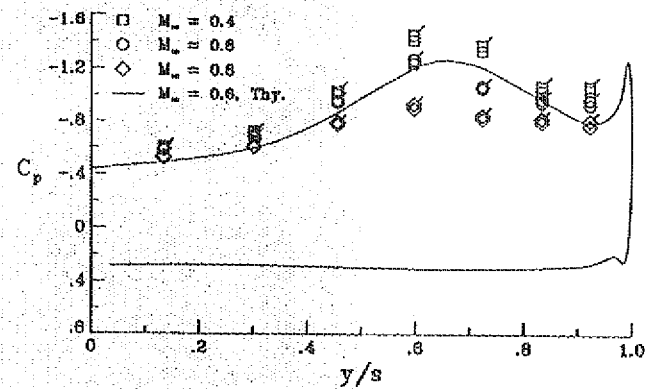
(d) Station 4, $\alpha = 20°$.

Figure 10.- Experimental sensitivity of surface C_p. $R_c = 0.8 \times 10^6$.
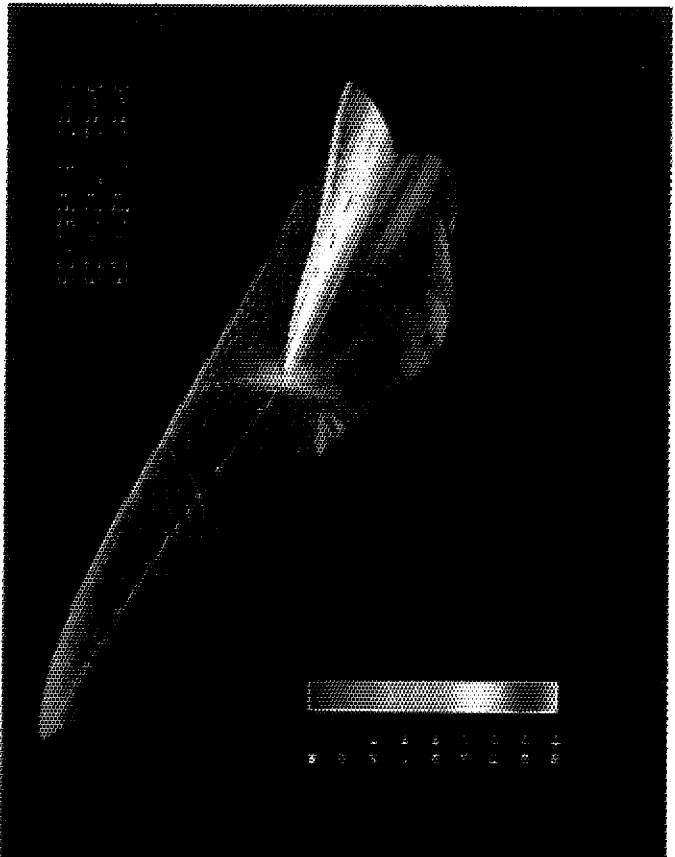
(b) Refined grid.

(a) Baseline grid.

Figure 11.- Static surface pressure coefficient contours. $M_\infty = 0.34$, $R_c = 13.5 \times 10^6$, $\alpha = 19°$.
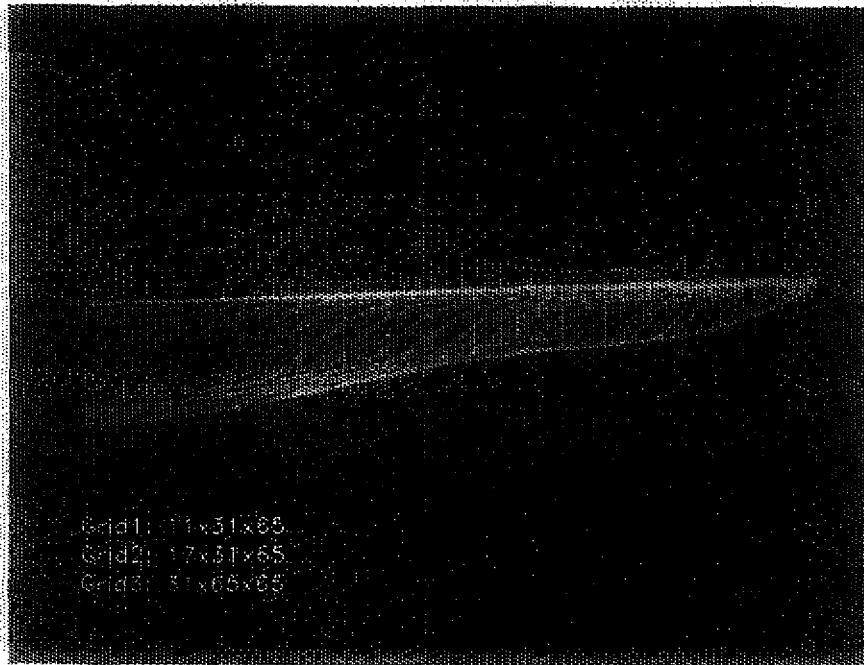
(a) Baseline grid.
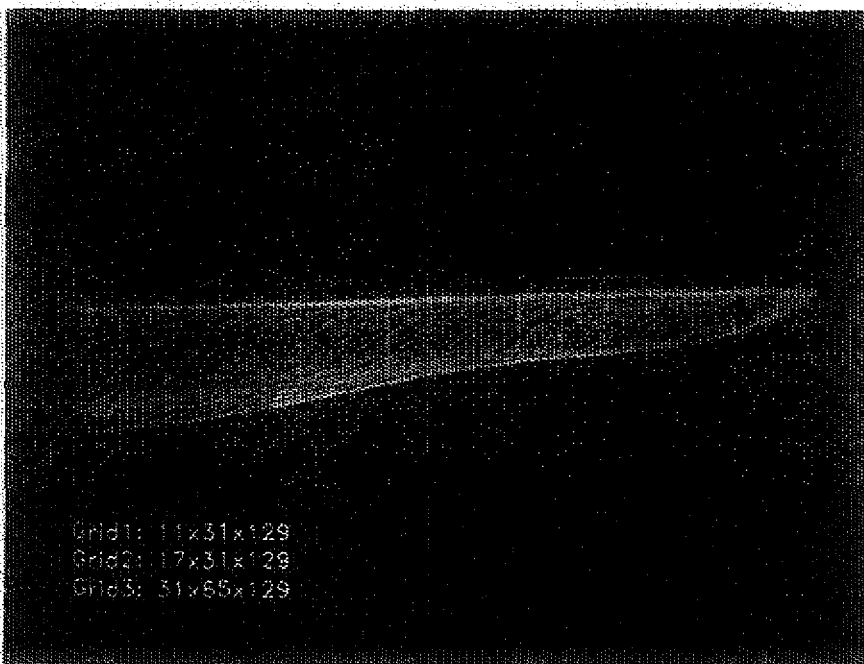
(b) Refined grid.

Figure 12.- LEX upper-surface flow pattern. $M_\infty = 0.34$, $R_{\bar{c}} = 13.5 \times 10^6$, $\alpha = 19°$.
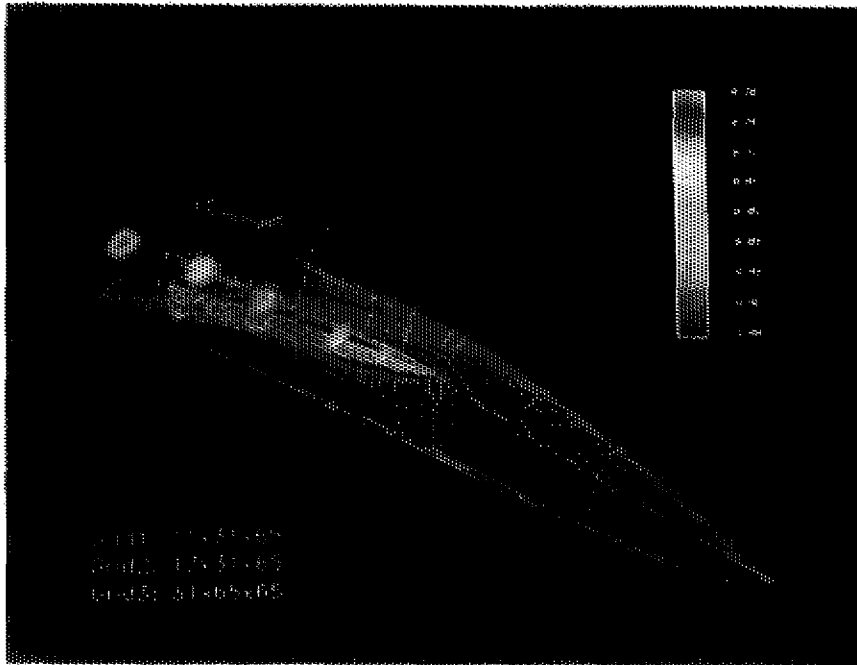
(a) Overall view.
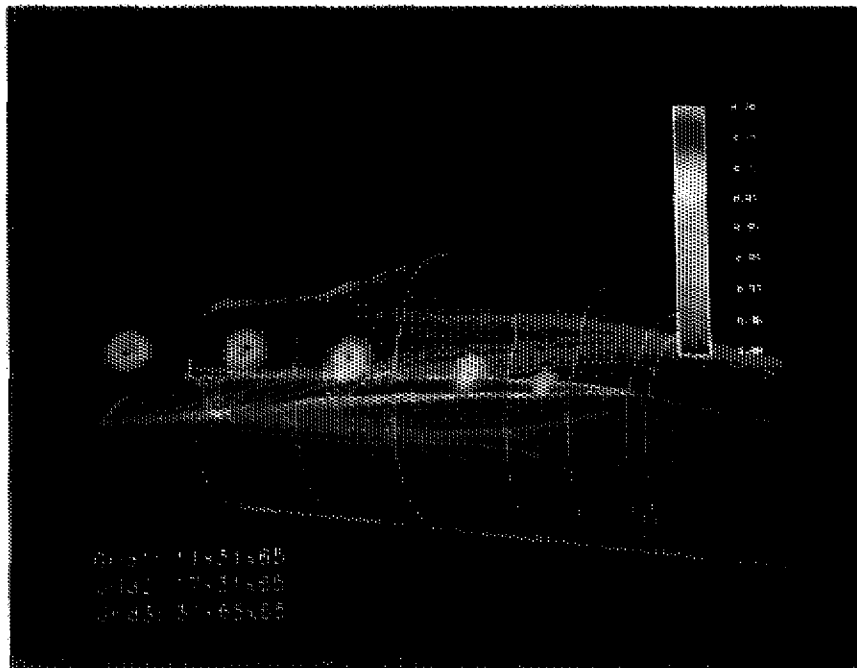
(b) LEX-body detail.

Figure 13.- Total pressure contours with surface flow pattern. $M_\infty = 0.34, R_c = 13.5 \times 10^6, \alpha = 19°$.
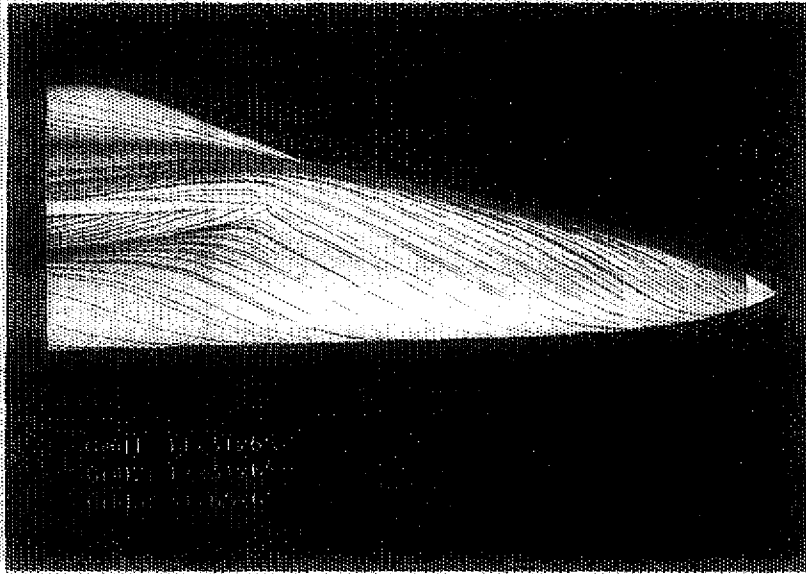
(a) Computational result.
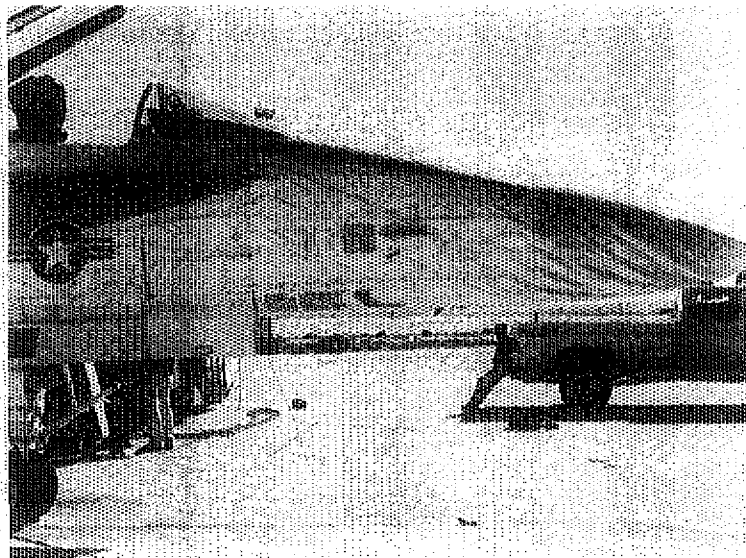
(b) Flight test.

Figure 14.- Comparison of computed turbulent surface streamlines with flight test - side view.
$M_\infty = 0.34$, $R_c = 13.5 \times 10^6$, $\alpha = 19°$.
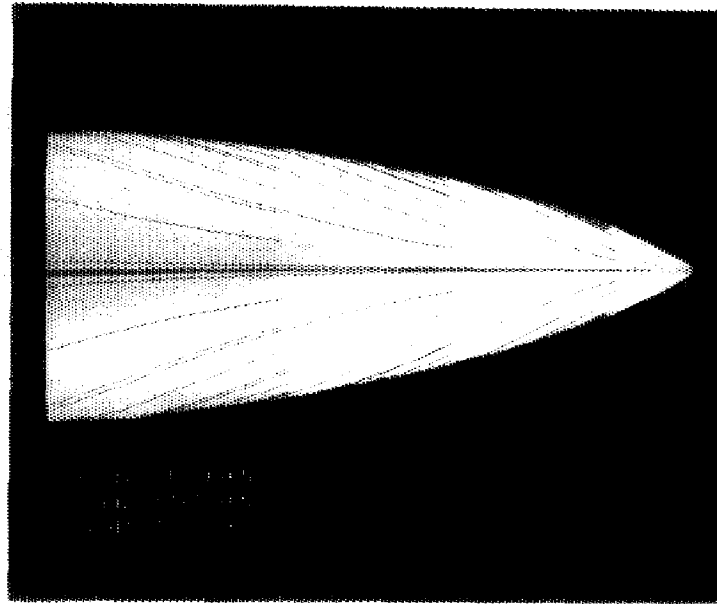
(a) Computational result.
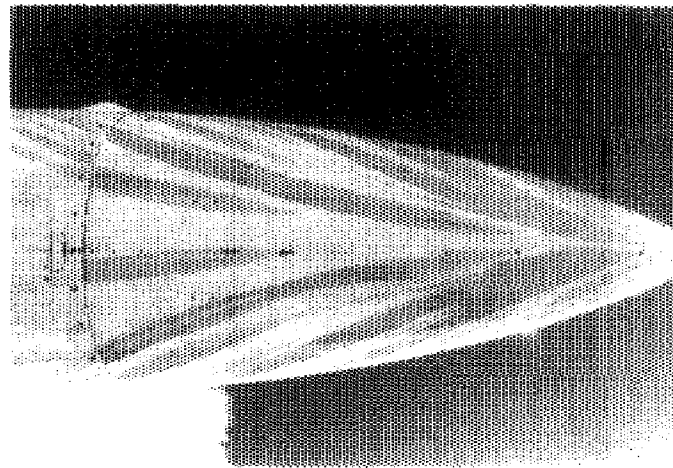
(b) Flight test.

Figure 15.- Comparison of computed turbulent surface streamlines with flight test - bottom view.
$M_\infty = 0.34, R_b = 13.5 \times 10^6, \alpha = 19°$.